The influence of iron impurities on the compression behavior of Al-2.24Mg-2.09Li alloy

Kozina, Franjo; Zovko Brodarac, Zdenka; Petrič, Mitja; Penko, Andrej

Source / Izvornik: **Journal of mining and metallurgy, Section B, Metallurgy, 2022, 56, 425 - 433**

Journal article, Published version
Rad u časopisu, Objavljena verzija rada (izdavačev PDF)

Permanent link / Trajna poveznica: https://urn.nsk.hr/urn:nbn:hr:115:635166

Rights / Prava: In copyright / Zaštićeno autorskim pravom.

Download date / Datum preuzimanja: **2024-12-02**

SVEUČILIŠTE U ZAGREBU METALURŠKI FAKULTET
UNIVERSITY OF ZAGREB FACULTY OF METALLURGY

Repository / Repozitorij:

Repository of Faculty of Metallurgy University of Zagreb - Repository of Faculty of Metallurgy University of Zagreb

DIGITALNI AKADEMSKI ARHIVI I REPOZITORIJI

J. Min. Metall. Sect. B-Metall., 56 (3) (2020) 425 - 433

Journal of Mining and Metallurgy,
Section B: Metallurgy

THE INFLUENCE OF IRON IMPURITIES ON THE COMPRESSION BEHAVIOUR OF Al-2.24Mg-2.09Li ALLOY

F. Kozina [a,*], Z. Zovko Brodarac [a], M. Petrič [b], A. Penko [b]

[a] University of Zagreb, Faculty of Metallurgy, Sisak, Croatia
[b] University of Ljubljana, Faculty of Natural Sciences and Engineering, Ljubljana, Slovenia

(Received 13 June 2020; Accepted 22 December 2020)

Abstract

As a major impurity element in aluminium-lithium (Al-Li) alloys, iron (Fe) reduces formability, fracture toughness, and fatigue resistance by solidifying into Al_6Fe and Al_3Fe particles. The research was performed in order to estimate the influence of Fe impurities on the compression behaviour of Al-2.24Mg-2.09Li alloy. The investigation was performed on the samples in as cast and solution hardened condition. The solution hardening was applied to improve the mechanical properties by dissolving intermetallic particles and enriching α_{Al} matrix with Mg. However, the higher strength properties and temperature increase during the compression testing were observed in as cast condition. Microstructural investigation revealed significant differences in microstructure changes between the samples in as cast and solution hardened condition. In as cast sample the barrelling effect led to the unequal deformation and surface texture development. The eutectic Al_3Fe particles located in the α_{Al} interdendritic areas did not significantly impact microstructure changes. Although the solution hardening led to enrichment of α_{Al} matrix with Mg and Fe, the Al_3Fe particles were not dissolved. The coarse morphology of Al_3Fe particles and location at the grain boundaries of α_{Al} grains contributed to low energy intergranular fracture. The fracture nucleation and propagation across the grain boundaries resulted in lower strength values.

Keywords: *Al-Mg-Li alloy; Iron impurities; Solution hardening; Compression testing; Microstructure; Low energy intergranular fracture*

1. Introduction

The aluminum (Al) – lithium (Li) alloys are characterized by density reduction, stiffness increase, increase in fracture toughness, fatigue crack growth resistance, and corrosion resistance [1]. The good engineering properties enable Al-Li alloys to contend with high strength 2xxx and 7xxx series of wrought Al alloys. Compared to copper (Cu) and zinc (Zn), Li additions enable direct density reduction (approximately 3% for every 1% of Li added) and increase in modulus of elasticity (approximately 6% for every 1% of Li added) improving specific strength and stiffness [2].

The limited utilization of Al-Li alloys stems from poor ductility, low fracture toughness, and high anisotropy of mechanical properties [3]. The embrittlement mechanism and susceptibility towards low energy intergranular fracture originate from chemical composition, microstructure developed during thermo-mechanical processing [4, 5] and sensitivity to deleterious impurities [6]. The major impurities found in Al-Li alloys are iron (Fe), silicone (Si), manganese (Mn), and alkaline elements [7]. The impurities are introduced through the addition of raw materials [8] and refractory pickup [9]. By segregating at the grain boundaries and solidifying or precipitating as secondary phase particles, the impurities enhance stress concentration sensitivity [10] and enable crack initiation [3]. Alkaline metal impurities, such as sodium (Na) and potassium (K), facilitate embrittlement by segregating at the grain boundaries and solidifying as low melting eutectic particles [7, 11]. The Fe impurities enable solidification of Al_6Fe and Al_3Fe particles. In binary Al-Fe systems the solidification of metastable Al_6Fe particles is only associated with cooling rates above 1 K/s [12]. In ternary Al-Li-Fe alloys the secondary Al_6Fe particles nucleate at pre-existing clusters in the liquid at 1.5wt.% Fe and temperatures above the liquidus [13]. Since they are finely distributed and localized in the centre of primary branches of α_{Al} dendrites [14, 15], the secondary Al_6Fe particles with globular morphology have no significant impact on the mechanical properties of an alloy [16]. As the Fe solubility in α_{Al} solid solution reduces to 0.0023wt.%

*Corresponding author: fkozin@simet.hr

https://doi.org/10.2298/JMMB200613038K

CC BY SA

at 580°C [17], the Fe segregates into the interdendritic areas of α_{Al} dendrites and enables solidification of eutectic Al_3Fe particles. The secondary eutectic Al_3Fe particles begin to solidify at the temperature of 590°C and cooling rate lower than 55K/s [18]. Due to the needle morphology and tendency towards coarsening, the Al_3Fe particles have detrimental effect on fracture toughness and fatigue resistance [16]. Furthermore, Al_3Fe particles are brittle and tend to crack and form notches during plastic deformation and processing [19].

The goal of the research is to estimate the influence of Fe impurities on the compression behaviour of Al-2.24Mg-2.09Li alloys in as cast and solution hardened condition. Since the improvement in strength properties of Al-Li-Mg alloys is mainly achieved through the solid solution hardening [20], the heat treatment was used in order to enrich α_{Al} matrix with Mg [21]. The solution hardening parameters were estimated based on thermodynamic behaviour of the Al-2.24Mg-2.09Li alloy [22].

2. Experimental

The alloy containing 2.24wt.% Mg and 2.09wt.% Li was synthesized in an induction melting furnace under vacuum. The Al block of commercial purity (99%) was placed into a graphite crucible coated with ferro-oxide and deposited into induction melting furnace. In order to eliminate the presence of impurity elements originating from raw materials, the alloying was performed using Mg rod of 99.98% purity and Li rod of 99.8% purity. The Mg and Li were wrapped in Al-foil (commercial purity) and placed into a steel bell coated with boron-nitrate. After achieving the vacuum of 300 Pa the Al block was melted. The alloying was performed at the temperature of 720°C by introducing previously prepared steel bell into the melt. Homogeneous distribution of alloying elements was ensured through additional reheating of the melt and steering with steel bell. The alloy was cast into a permanent steel mould at 740°C and atmospheric pressure.

The Mg and Li content were determined using inductively coupled plasma with mass spectroscopy on Agilent Technologies Inductively coupled plasma - mass spectrometer (ICP). Due to the high reactivity of Li, the ICP was calibrated using solutions containing 1, 10, 50, and 100 mg/m^3 of Li. The Fe content was measured by spectroscopy on Labeco GDS900 SPECT W spectrometer. The spectrometer was calibrated using two different certified referent materials for Al-based alloys.

The compression testing was performed on the samples in as cast and solution hardened condition using Gleeble 1500D thermo-mechanical simulator. The sample was solution hardened at 520°C for 4h and quenched in water. The sample in as cast condition was compressed at the room temperature, while the solution hardened sample was compressed at the temperature of 190°C. The testing temperature was achieved in 50s. However, to obtain even distribution of the heat, the sample was kept at the testing temperature for 5min before initiating the compression testing. The samples with initial length of 10.0 mm and diameter of Ø6.0 mm, were compressed using Gleeble 1500D thermo-mechanical simulator. During compression testing the force was increased from 0 N to almost 30 000 N with the strain rate of 25 s^{-1}. The strain rate was constant during the testing. The compression was conducted with the data acquisition rate of 10 000 Hz during testing without any additional corrections of obtained data after testing. The influence of friction was limited by using tantalum foil and nickel-based paste between sample and Gleeble working jaws. In order to determine the strength properties, the samples were compressed till 0.7 deformation was reached. The obtained engineering stress-strain curves were used to determine yield strength, upper yield point, lower yield point, compression strength, and ultimate point. At the yield strength point the engineering strain started to increase faster than engineering stress because of the initiation of inelastic deformation. After reaching the yield strength the samples started to exhibit plastic behaviour. At the upper yield, the maximum loading was required to initiate the plastic deformation causing the engineering stress increase. After reaching its maximum, the plastic deformation of the material required minimum loading. This drop in engineering stress was registered as lower yield point. The compressive strength represented the maximum engineering stress till 0.7 deformation was reached. The ultimate point represented the engineering stress at which the 0.7 deformation was reached or the sample brakes. Measuring the sample before and after compression testing enabled area reduction calculation. Surface temperature change was monitored during compression testing.

The metallographic analysis was performed on the samples in as cast and solution hardened conditions, before and after compression. The samples were prepared using standard grinding and polishing technics. The samples for macrostructural analysis were etched using Poulton's etching solution containing 60 ml of hydrochloric acid (HCl), 30 ml of nitric acid (HNO_3), 5 ml of hydrofluoric acid (HF), and 5 ml water. Macrostructure was observed on stereo microscope Olympus SZ11. The samples for microstructural analysis were etched using Weck's etching solution consisting of 4 g $KMnO_4$, 1 g NaOH, and 100 ml H_2O. The microstructure was analysed on Olympus GX51 inverted metallographic microscope equipped with AnalySIS Materials Research Lab

software support. The scanning electron microscope Tescan, Vega TS 5136 MM equipped with energy dispersive spectrometer (EDS) was used to locate and quantify Fe impurities in microstructure of the analysed samples.

3. Results and discussion

The chemical composition of the synthesized alloy is given in Table 1.

Table 1. *Chemical composition of the alloy*

Mg/wt.%	Li/wt. %	Fe/wt.%	Al/wt.%
2.244	2.093	0.157	balance

The synthesized alloy contained 2.244wt.% Mg, 2.093wt.% Li, and 0.157wt.% Fe. The presence of Fe impurities was a result of refractory pickup during melting of the alloy.

The macrostructure of the samples in as cast and solution hardened condition is given in Figure 1.

The macrostructure of the sample in as cast condition exhibited heterogeneous grain morphology consisting of chill, columnar, and equiaxed zones. The narrow chill zone with an average thickness of 0.21mm was formed at the surface of the sample, followed by zone of columnar grains with an average thickness of 1.32mm (Figure 1 a). The zone of equiaxed grains was in the centre of the sample and had the largest average thickness of 26.94mm (Figure 1 b). The solution hardening led to the homogenization in the grain morphology (Figure 1 c) without an increase in the grain size (Figure 1 d).

The microstructure of the samples in as cast and solution hardened condition is shown in Figure 2 a and b, while the Scanning Electron Images (SEI) with the details for EDS analysis are given in Figure 2 c and d. The following EDS analysis is presented in Table 2.

Table 2. *The EDS analysis results for the details in Figure 2*

Condition	Detail	Al/wt.%	Mg/wt.%	Fe/wt.%
As cast	1	93.12	2.63	0.34
	2	94.03	5.20	0.52
	3	83.36	3.96	12.27
Solution hardened	1	92.99	5.56	0.44
	2	92.80	6.25	0.51
	3	80.36	4.2	13.44

Microstructure of the as cast sample revealed α_{Al} dendritic network (Figure 2 a) consisting of 93.12wt.% Al, 2.63wt.% Mg, and 0.34wt.% Fe (Figure 2 c, detail 1, Table 2 detail 1). Reduced solubility, led to the Fe segregation into interdendritic areas and increase in Fe content to 0.52wt.% (Figure 2 c, detail 2, Table 2 detail 2). The EDS analysis indicated presence of Fe-based intermetallic particles

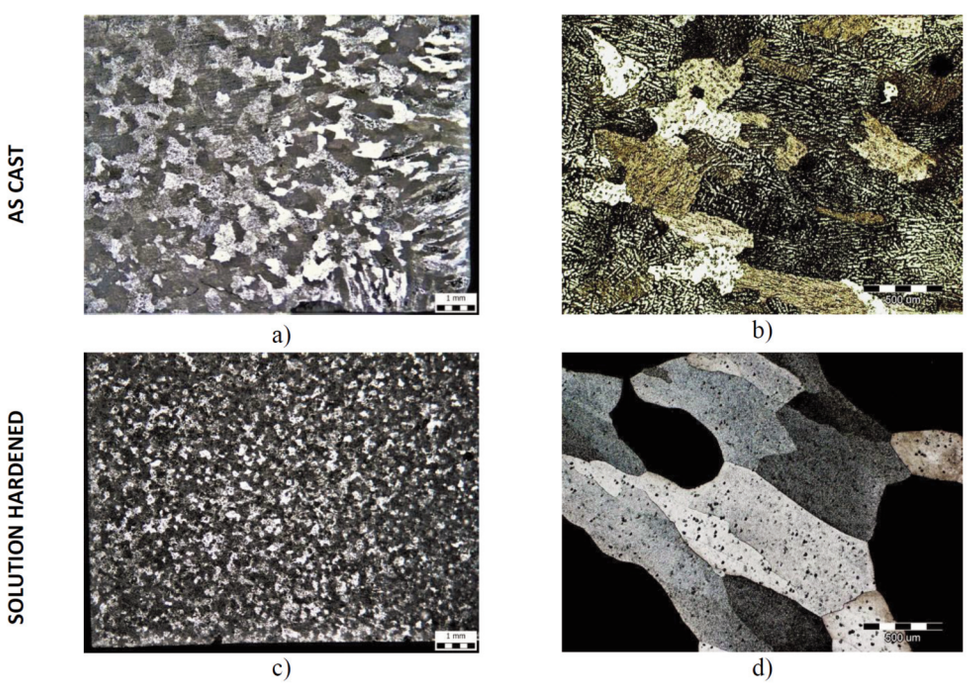

Figure 1*. The macrostructure of the samples in: a) as cast condition at 15X, b) as cast condition at 50X, c) solution hardened condition at 15X, d) solution hardened condition at 100X*

CC BY SA

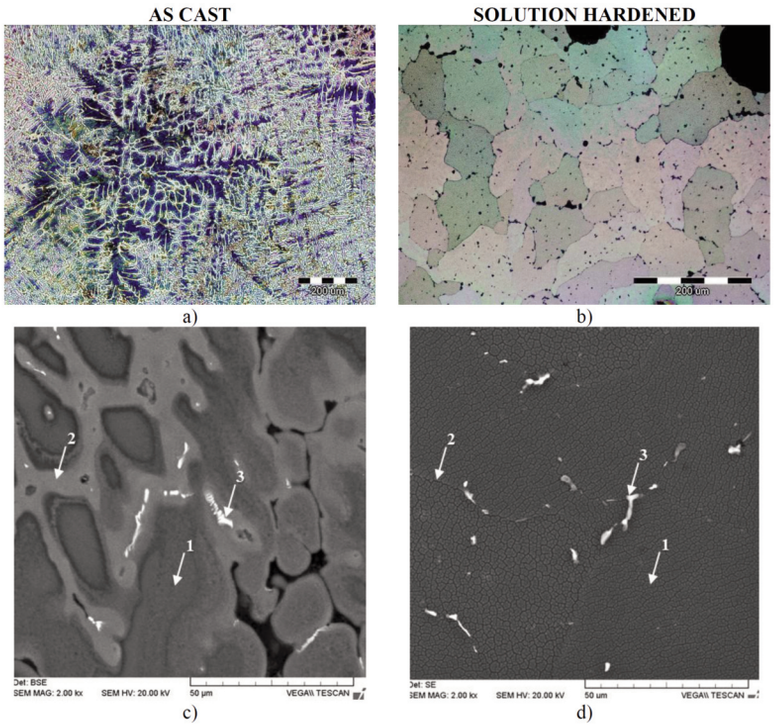

Figure 2. *The microstructure of the samples in: a) as cast condition, b) solution hardened condition, c) SEI in as cast condition, d) SEI in solution hardened condition*

containing 83.36wt.% Al, 12.27wt.% Fe, and 3.96wt.% Mg (Figure 2 c detail 3, Table 2 detail 3).

The microstructure of the solution hardened sample revealed α_A grains (Figure 2 b). The content of Mg and Fe in the α_{Al} solid solution increased to 5.56wt.% Mg and 0.44wt.% Fe due to solution hardening (Figure 2 d, detail 1, Table 2 detail 1). However, α_{Al} grain boundaries still contained higher amount of Mg and Fe (Figure 2 d, detail 2, Table 2 detail 2). The Fe-based intermetallic particles containing 80.36wt.% Al, 13.34wt.% Fe, and 4.72wt.% Mg (Table 2 detail 3) were found at the grain boundaries (Figure 2 d detail 3). The located particles correspond to Al_3Fe precipitates.

The engineering strain-stress curves for the as cast and solution hardened sample are given in Figure 3, while the results of compression testing are shown in Table 3, respectively.

During compression testing the sample in as cast condition started to exhibit inelastic deformation behaviour at 233.91 MPa (Figure 3 a). The initial length of the sample started to reduce at the point of 293.03 MPa (Table 3). After the compression strength dropped to 116.31 MPa the initial length of the sample

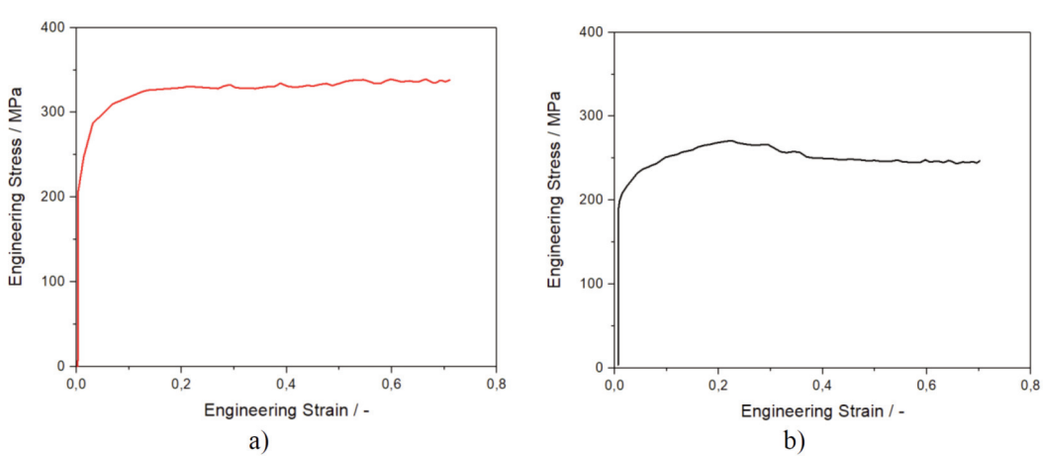

Figure 3. *The engineering strain-stress curves for the samples in: a) as cast condition, b) solution hardened condition*

CC BY SA

Table 3. *Results of compression testing*

Condition	Yield strength/MPa	Upper yield point, MPa	Lower yield point, MPa	Compression strength/MPa	Ultimate point/ MPa	Area reduction/%	Temperature increase/°C
As cast	233.91	293.03	116.31	341.36	338.18	50	69.0
Solution hardened	249.49	288.07	211.56	287.31	246.98	20	30.0

was reduced with little increase in engineering stress. The as cast sample achieved the ultimate compression strength of 341.36 MPa (Table 3). The sample yielding was recorded in the engineering strain rage of 0.027 – 0.364 (Figure 3 a). The compression testing stopped at ultimate point of 338.18 MPa (Table 3) when the sample was reduced for 50% of its initial length.

The inelastic deformation behaviour of the solution hardened sample started at 249.49 MPa (Figure 3 b). The initial length of the sample started to reduce at the upper yield point of 288.07 MPa (Table 3). The yielding of the solution hardened sample started at lower yield stress point of 211.56 MPa and ended at ultimate compression strength of 287.31 MPa (Table 3). The compression testing stopped at 246.98 MPa after the sample broke (Figure 3 b).

The increase in deformation energy during compression increased the temperature of the samples. The engineering strain-temperature curves for as cast and solution hardened sample are given in Figure 4 a and b.

The temperature of both samples increased with the increase in engineering strain (Figure 4). Both samples achieved its maximum temperature increase at the engineering strain of 0.74. The temperature of the sample in as cast condition increased for 69.0°C at 338.6 MPa. The temperature of the solution hardened sample increased for 30.0°C at the compression strength of 240.02 MPa (Figure 4).

The sample in as cast condition was reduced for 50% of its initial length (Table 3, as cast). The solution hardened sample was reduced for 20% of its initial length (Table 3, solution hardened).

The Figure 5 shows the macrostructure of the surface parallel to the compression direction.

The macrostructure of the compressed sample in as cast condition indicated the unequal deformation and barrelling effect (Figure 5 a). The measurements performed on the macrostructure (Figure 5 a) indicated 49.56% less deformation at the surface part of the sample (Figure 5 a, detail 1) compared to the sample's middle (Figure 5 a, detail 2). The compression of the solution hardened sample caused the slip formation and cracking (Figure 5 b). The fracture has occurred at the 45° angle between fracture surface and the loading direction indicating the highest shear stress zone (forging cross zone) (Figure 5 b).

The microstructure of the sample in as cast condition after compression is given in Figure 6.

The microstructure analysis of as cast sample after compression testing indicated unequal deformation (Figure 6). More significant deformation of the α_{Al} dendrites near the surface of the sample resulted in the surface texture development with the average thickness of 808.89 μm. The α_{Al} dendrites were elongated perpendicular to the deformation direction (Figure 6 a). The α_{Al} dendrites located near the middle part of the cross section showed less deformation (Figure 6 b). The overlapping of material was detected at the surface of the part of the sample subjected to the highest deformation (Figure 6 c). The progression of the

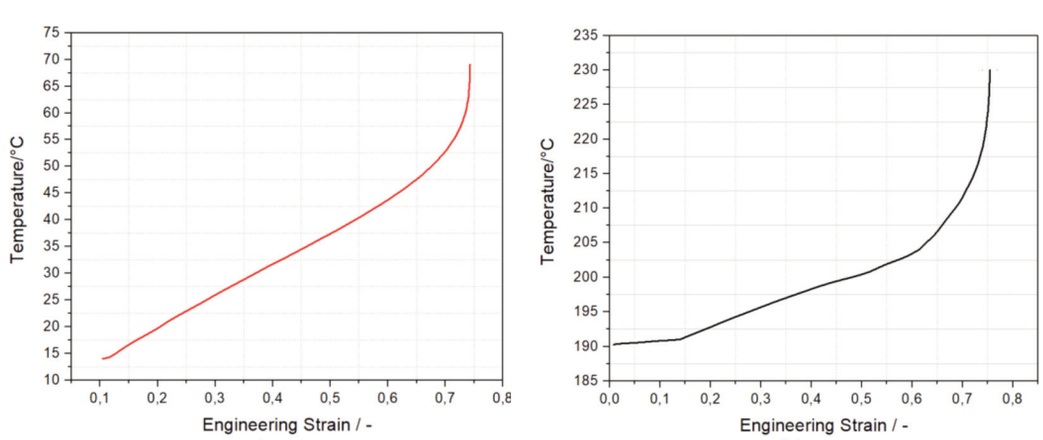

Figure 4. *The engineering strain-temperature curves for the samples in: a) as cast condition, b) solution hardened condition*

CC BY SA

overlapping indicated equal involvement of α_{Al} dendritic network and interdendritic areas (Figure 6 d).

The Figure 7 shows the microstructure of the solution hardened sample after compression.

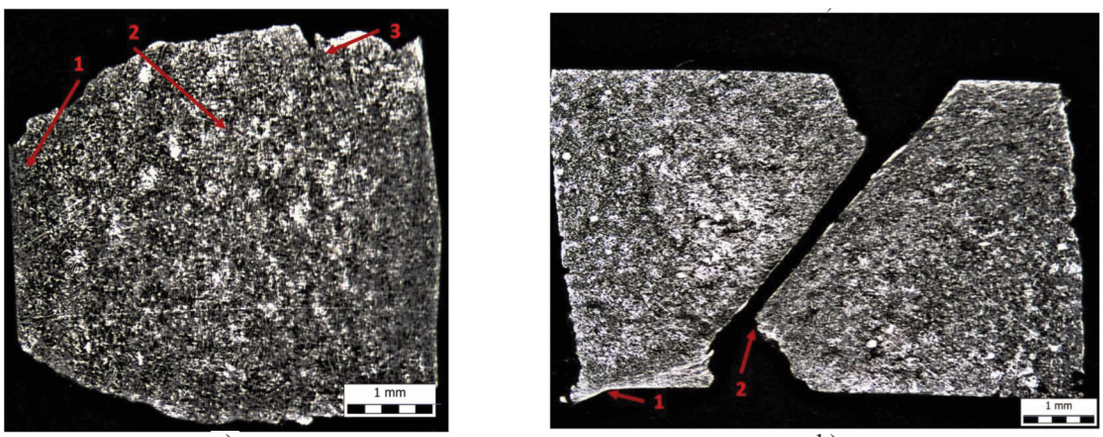

a) b)

Figure 5. *The macrostructure of the compressed samples with indicated details for microstructural analysis: a) as cast condition, b) solution hardened condition*

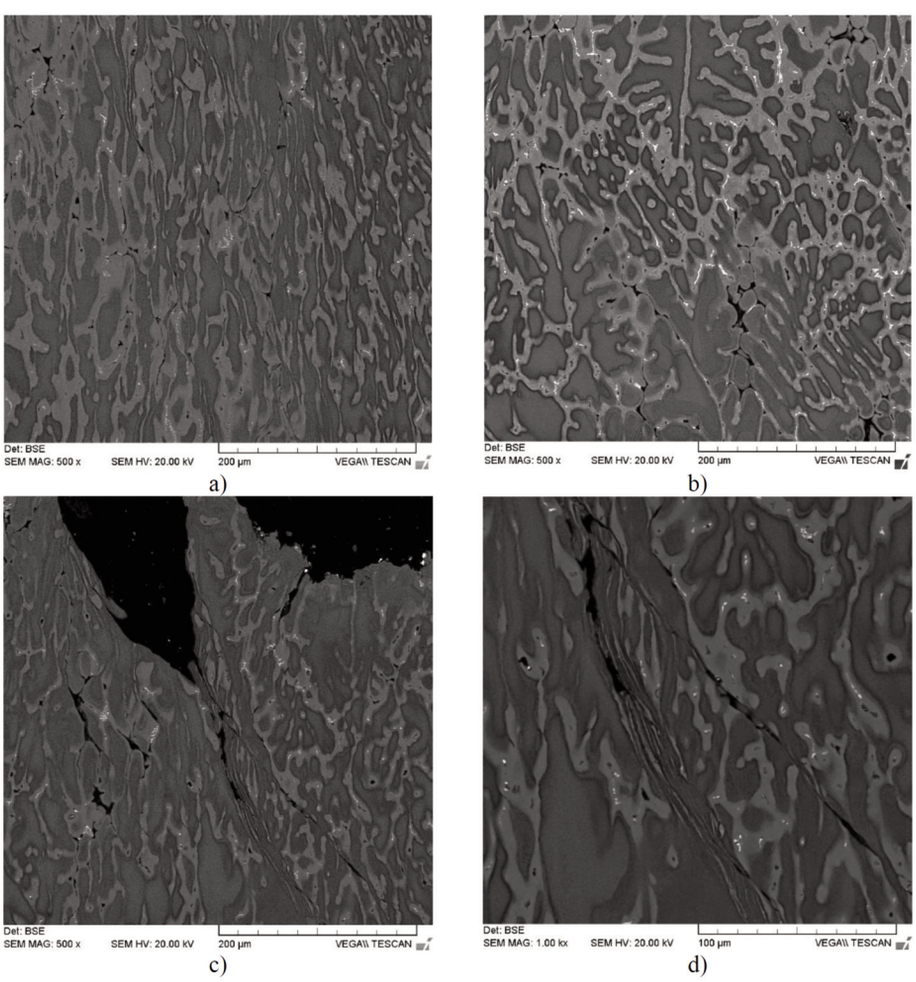

Figure 6. *The microstructure of the sample in as cast condition at the details indicated in Figure 5 a: a) detail 1, b) detail 2 c) detail 3, and d) overlapping progression*

CC BY SA

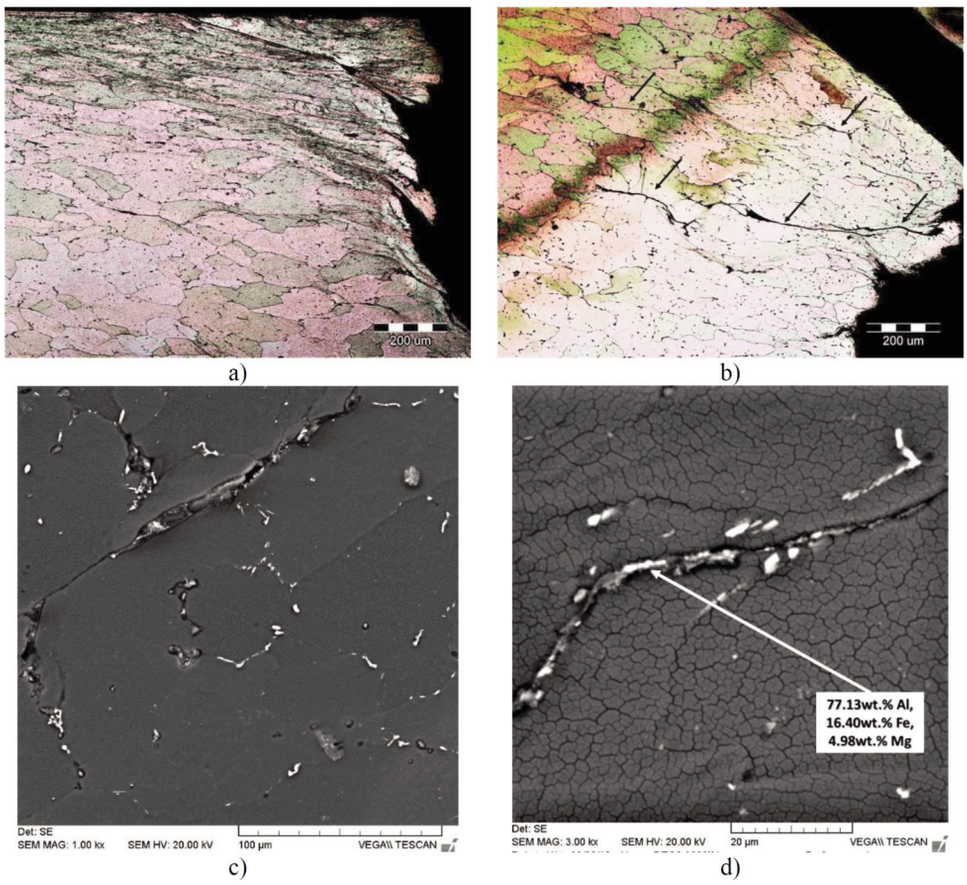

Figure 7. *The microstructure of the solution hardened sample after compression: a) surface of the sample (Figure 5 b, detail 1), b) progression of the low energy intergranular fracture (Figure 5 b, detail 2), c) grain boundary involvement in fracture progression, d) the Fe-based intermetallic particles located in the fracture*

The microstructural analysis of the compressed solution hardened sample indicated unequal deformation of the surface grains and grains in the centre of the sample (Figure 7 a). The low energy intergranular fracture nucleated at the surface of the sample and progresses across the grain boundaries towards the sample centre (Figure 7 b, c). The grains located near the fracture showed no change in morphology (Figure 7 b). The SEM and EDS analysis of the fracture indicated the presence of Fe-based intermetallic particles containing 77.13wt.% Al, 16.40wt.% Fe, and 4.98wt.% Mg (Figure 7 d) which corresponded to Al_3Fe particles.

4. Conclusions

The evaluation of the Fe impurity's influence on the compression behaviour of Al-2.24Mg-2.09Li alloy in as cast and solution hardened condition led to the following conclusions:

The Fe impurity pickup originated from ferro-oxide crucible coating and steel bell used during alloy synthesis. The reduced solid solubility of Fe in α_{Al} solid solution, resulted in solidification of Al_3Fe particles in the interdendritic areas of α_{Al} dendritic network.

The solution hardening enabled dissolution of α_{Al} dendritic network and formation of α_{Al} grains enriched with Mg and Fe. The Al_3Fe intermetallic particles located at the grain boundaries were not affected by solution hardening.

The as cast sample was compressed for 50% of its initial length with an increase in temperature for 69°C. The solution hardened sample cracked after it was compressed for only 20% of its initial length with the temperature increase of 30°C.

The barrelling effect of as cast sample led to the unequal deformation and surface texture development. The material overlapping initiated at the surface of the sample's middle and progressed with equal involvement of α_{Al} dendritic network and interdendritic areas.

The compression of the solution hardened sample resulted in low energy intergranular fracture. The fracture developed at the 45° angle regarding to the loading direction indicating the highest shear stress zone.

CC BY SA

The performed research indicated higher compression strength (341.36 MPa), ultimate point (333.98 MPa) and area reduction (50%) for the sample in as cast condition. Lower strength properties and temperature increase during compression of the solution hardened sample resulted from low energy intergranular fracture formation. The material weakening and fracture formation were enabled by solidification of coarse Al_3Fe particles at the grain boundaries of α_{Al} grains.

Acknowledgements

The investigation was performed within the research topic "Design and Characterization of Innovative Engineering Alloys", Code: FPI-124-2019-ZZB funded by University of Zagreb, within the Framework of Financial Support of Research, scientific-research project within Croatian-Slovenian collaboration "Design and Characterization of Innovative Aluminum - Magnesium - Lithium alloy (2018-2019) funded by Ministry of Science and Education and Infrastructural scientific projects: Center for Foundry Technology, Code: KK.01.1.1.02.0020 and VIRTULAB - Integrated Laboratory for Primary and Secondary Raw Materials, Code: KK.01.1.1.02.0022 funded by European Regional Development Fund, Operational programme Competitiveness and cohesion 2014 - 2020.

References

[1] R. J. Rioja, J. Liu, Metall. Mater. Trans. A Phys. Metall. Mater. Sci., 43 (9) (2012) 3325–3337.

[2] A. Gloria, R. Montanari, M. Richetta, A. Varone, Metals (Basel)., 9 (6) (2019) 1–26.

[3] X. Chen, G. Zhao, G. Liu, L. Sun, L. Chen, C. Zhang, J. Mater. Process. Technol., 275 (2020) 116348

[4] R. Goswami, N. Bernstein, Miner. Met. Mater. Ser., Part F4 (2018) 217–223.

[5] Z. Zovko Brodarac, T. Holjevac Grgurić, J. Burja, J. Therm. Anal. Calorim., 127 (1) (2017) 431–438.

[6] S. S. Nazarov, S. Rossi, P. Bison, I. Ganiev, L. Pezzato, I. Calliari, Phys. Met. Metallogr., 120 (4) (2019) 402–409.

[7] R. J. H. Wanhill, N. E. Prasad, A. A. Gokhale, Aluminum-Lithium Alloys: Processing, Properties, and Applications, Elsevier Inc., 2013.

[8] Y. Z. Di, J. P. Peng, Y. W. Wang, N. X. Feng, J. Min. Metall. Sect. B-Metall., 54 (3) B (2018), 369–375.

[9] J. Yuan, J. Pang, G. Xie, Y. Wang, L. Han, Metall. Mater. Trans. A Phys. Metall. Mater. Sci., 50 (3) A (2019) 1509–1521.

[10] Q. Gao, H. Zhang, R. Yang, Z. Fan,Y. Liu, J. Wang, X. Geng, Y. Gao, S. Shang, Y. Du, Z. Liu, J. Min. Metall. Sect. B-Metall., 54 (2) B (2018) 185–196.

[11] Y. Tao, B. L. Xiao, Z. Y. Ma, W. Wu, R. X Zhang, Y. S. Zeng, Mater. Sci. Eng. A, 693 (March) A (2017) 1–13.

[12] K. Hu, F. Yu, Q. Le, Metall. Mater. Trans. B-Process Metall. Mater. Process. Sci., 51, (2) B (2020) 697–708.

[13] F. H. Samuel, G. Champier, J. Mater. Sci., 23(2) (1988) 541–546.

[14] S. Manasijević, N. Dolić, Z. Zovko Brodarac, M. Djurdjević, R. Radiša, Metall. Mater. Trans. A, 45 (10) A (2014) 4580–4587.

[15] Z. Zovko Brodarac, F. Unkić, J. Medved, P. Mrvar, Kovove Mater., 50(1) (2012) 59-67.

[16] W. S. Ebhota, T.C. Jen, Intermetallic Compounds - Formation and Applications (M. Aliofkhazraei), InTech Open, London, 2018, p. 21-27.

[17] C. L. Liu, Q. Du, N. C. Parson, W. J. Poole, Scr. Mater., 152 (2018) 59–63.

[18] Y. L. Liu, Z. Q. Hu, Y. Zhang, C. X. Shi, Metall. Trans. B, 24, (5) B (1993) 857–865.

[19] J. Chen, C. Liu, R. Guan, F. Wen, Q. Zhou, H. Zhao, J. Mater. Res. Technol., 2019, doi: 10.1016/j.jmrt.2019.12.008.

[20] F. Kozina, Z. Zovko Brodarac, M. Petrič, 73rd World Foundry Congress WFC 2018 - Proceedings, 23-27.08.2018, Krakow, Poland, 2018, p. 21–22

[21] N. Dolic, Z. Zovko Brodarac, J. Min. Metall. Sect. B Metall., 53 (3) B (2017) 429–439.

[22] F. Kozina, Z. Zovko Brodarac, M. Petrič, B. Leskovar, CEEC-TAC5 & Medicta 2019 Book of Abstracts, 27-30.07.2019, Roma, Italy, 2019, p. 145–145.

UTICAJ PRIMESA NA BAZI ŽELEZA NA KOMPRESIVNE KARAKTERISTIKE Al-2.24Mg-2.09Li LEGURE

F. Kozina [a,*], Z. Zovko Brodarac [a], M. Petrič [b], A. Penko [b]

[a] Sveučilište u Zagrebu, Metalurški fakultet, Sisak, Hrvatska
[b] Univerzitet u Ljubljani, Fakultet za prirodnjačke i tehničke nauke, Ljubljana, Slovenija

Apstrakt

Kao glavna štetna primesa u aluminijum-litijum (Al-Li) legurama, železo (Fe) smanjuje sposobnost oblikovanja, žilavost loma materijala i otpornost na lom materijala usled zamora zbog očvršćavanja Al_6Fe i Al_3Fe čestica. Istraživanje je izvedeno u cilju procene uticaja prisustva štetnih Fe primesa na Al-2.24Mg-2.09Li leguru prilikom sabijanja. Ispitivanje je izvršeno na livenim i na rastvorno ojačanim uzorcima. Rastvorno ojačavanje je izvršeno zbog poboljšanja mehaničkih svojstava rastvaranjem intermetalnih čestica i obogaćivanjem α_{Al} matrice Mg. Međutim, veća čvrstoća i porast temperature su primećeni kod livenih uzoraka prilikom sabijanja. Ispitivanje mikrostrukture je pokazalo značajne razlike kod promene mikrostrukture između uzoraka koji su liveni i rastvorno ojačani. Barrelling efekat je kod livenog uzorka doveo do nejednake deformacije i promene teksture površine. Eutektičke čestice Al_3Fe koje se nalaze u interdendritičkim delovima αAl nisu imale značajan uticaj na promenu mikrostrukture. Iako je rastvorno ojačavanje dovelo do obogaćivanja α_{Al} matrice Mg i Fe, čestice Al_3Fe se nisu rastvorile. Gruba morfologija Al_3Fe čestica i njihov položaj na granicama zrna α^{Al} su doprineli pojavi niskoenergetskog međugranularnog loma. Nukleacija loma i širenje preko granica zrna su bili uzrok nižih vrednosti dobijenih za čvrstoću.

Ključne reči: *Al-Mg-Li legura; Štetne primese gvožđa; Kaljenje; Sabijanje; Mikrostruktura; Niskoennergetski međugranularni lom*

CC BY SA